

Interaction of Turbulent Barotropic Shallow-Water Flow With Topography

Alexander. F. Shchepetkin¹

Center for Ocean-Atmospheric Prediction Studies²,
Florida State University, 020 Love Bldg., Tallahassee, FL 32306-3041

Abstract. It was recognized recently that the interaction of the mesoscale eddy field with bottom topography of the the ocean does not only lead to the dissipation of large scale ocean currents, but may appear as a driving force that strongly affects the large scale circulation. A high resolution numerical model is employed to investigate the evolution of the turbulent eddy flow over topography. Our attention is focused on the extreme case, when the change of layer depth is comparable to its maximum value. Under these conditions the flow is primarily controlled by the vorticity dynamics, particularly by the stretching of vorticity lines and the tendency to conserve potential vorticity. Because the cross-isobatic motion of fluid particles causes changes of the relative vorticity comparable to the local Coriolis parameter, the flow is no longer in the geostrophic regime. The particular goal is to explore the mechanisms of large-scale rectified flow emerging from an initial random eddy field. Several numerical experiments with the barotropic shallow water model were performed with low dissipation and with idealized geometry and topography were performed.

Introduction

Rhines and Young (1982a,b) presented a quasi-geostrophic (QG) theory of the wind-driven circulation in the presence of bottom topography. This theory combines the ideas of topographic forcing of the fluid motion and of homogenization of the potential vorticity field by mesoscale eddy interaction. The topographic forcing results in the tendency that water parcels move along the contours of *constant planetary potential vorticity*, i.e., f/H lines, where f is the *local* Coriolis parameter and H is the depth. Earlier numerical experiments by Rhines (1975) investigate the development of geostrophic turbulence in a periodic domain in the presence of β -effect and topography. It was found that the planetary β -effect partially inhibits the eddy merger process, restricting the maximum scale to which the coherent structures may grow to (Rhines' rule)

$$k_{\min} = \sqrt{\frac{\beta}{\sqrt{\langle u^2 \rangle}}}, \quad (1)$$

where k_{\min} is the minimum wavenumber associated with the streamfunction or the potential vorticity (PV) field, while $\sqrt{\langle u^2 \rangle}$ is the mean square velocity of the random field.

A theoretical study by Carnevale and Frederiksen (1986) applies Arnold's criterion to the nonlinear stability properties of QG flows over topography. It was shown that minimum enstrophy states have potential vorticity proportional to the streamfunction and are nonlinearly stable.

In the spirit of the quasigeostrophic theory, the effects of bottom topography were always treated as modification to the β -effect, e.g., Salmon *et al.*, 1976. This theory makes a qualitative distinction between regions where lines $f/H = \text{const}$ intersect the boundaries of the domain and regions of closed f/H contours. In the latter case the geostrophic flow is topographically trapped and the potential vorticity tends to homogenize (Rhines and Young 1982b). A similar effect was observed by Thompson (1993) in a numerical experiment with a QG eddy-resolving three-layer model, which shows the emerging of abyssal cyclonic circulation in the region where f/H contours

¹ Author affiliation and corresponding address effective from May 1, 1995: Institute of Geophysics and Planetary Physics, University of California at Los Angeles, 405 Hilgard Avenue, Los Angeles, CA 90024-1567

² Formerly known as Mesoscale Air-Sea Interaction Group (MASIG)

are closed.

On the other hand, coarse resolution numerical models used in climatological studies cannot simulate the effect of the self-organization of the random eddy-field into large scale motion over topography. Holloway proposed to parametrize this subgrid scale effect by relaxing the velocity field to some *nonrest* final state, \mathbf{u}_* , i.e. the conventional dissipation in the right hand side of the momentum equations is replaced by terms like

$$\frac{\mathbf{u} - \mathbf{u}_*}{\tau} \quad \text{or} \quad A\Delta(\mathbf{u} - \mathbf{u}_*), \quad (2)$$

where τ is a relaxation time and \mathbf{u}_* is some function of the bottom slope (Holloway 1986, Eby and Holloway 1994, Cummins and Holloway 1994, Holloway and Eby 1994, Alvarez *et al.* 1994).

Several questions remain open.

- The QG theory always assumes that the disturbances of the bottom topography are small in comparison with the characteristic depth. In reality, however, the depth changes continuously from the deep ocean to coastal regions, where it is nearly zero. Consequently, the f/H contours are *always closed*.

- As it was pointed out above, there is the expectation that mesoscale eddy mixing drives the flow to the statistically equilibrium state predicted by the minimum enstrophy principle, but the particular dynamical mechanism of this process and its characteristic time scale remain unexplored.

- It is also not clear how close real flows are to the equilibrium state and to what extent the existent models can simulate this effect directly or must rely on parametrizing it.

In the present study we attempt to simulate the eddy-topography interaction in the simplest case, in the absence of wind forcing and with idealized geometry and topography. Most of the previous theoretical studies are made within the QG framework, while their results were applied to primitive equation models. We chose the barotropic shallow-water equations over finite amplitude bottom topography as the prototype system. This model is free of the restrictions typical for QG models.

Barotropic Shallow-Water Equations With Bottom Topography

Consider the barotropic one-layer shallow water equations with bottom topography, in Cartesian co-

ordinates:

$$\begin{aligned} \frac{\partial U}{\partial t} + \frac{\partial P_{xx}}{\partial x} + \frac{\partial P_{xy}}{\partial y} - fV &= -H \frac{\partial p}{\partial x} \\ \frac{\partial V}{\partial t} + \frac{\partial P_{xy}}{\partial x} + \frac{\partial P_{yy}}{\partial y} + fU &= -H \frac{\partial p}{\partial y} \\ \frac{\partial R}{\partial t} + \frac{\partial U}{\partial x} + \frac{\partial V}{\partial y} &= 0 \end{aligned} \quad (3)$$

where upper case $U = \rho H u$, $V = \rho H v$ are the mass fluxes in x and y directions; lower case u and v are the velocities; H is the layer thickness; ρ is the density of the fluid; $R = \rho H$ is vertically integrated *mass content*, or the two-dimensional density; $p = \rho g(H - D)$ is the pressure field obtained from the hydrostatic equation, g is the acceleration of gravity, and D is the layer thickness at rest. P_{xx} , P_{xy} and P_{yy} are the components of the *tensor of the momentum flux*, and they are defined as follows:

$$\begin{aligned} P_{xx} &= Uu - AR\left(\frac{\partial u}{\partial x} - \frac{\partial v}{\partial y}\right) \\ P_{yy} &= Vv + AR\left(\frac{\partial u}{\partial x} - \frac{\partial v}{\partial y}\right) \\ P_{xy} = P_{yx} &= \frac{1}{2}(Uv + uV) - \\ &\quad - AR\left(\frac{\partial v}{\partial x} + \frac{\partial u}{\partial y}\right) \end{aligned} \quad (4)$$

where A is the horizontal friction coefficient. This definition of the momentum flux tensor is somewhat nonstandard because the pressure term has been excluded. This is done for convenience because the pressure term will always be considered separately in the numerical discussion. The expression for the nonlinear term in the bottom line of eqns (4) looks redundant, because obviously $Uv = uV = Ruv$. However, as we will see soon, this equality will no longer be valid in the discrete case, if a staggered grid is used to discretize eqns (3).

An Arakawa C -grid is used to discretize eqns (3). In our elementary stencil $V_{j,k}$ is located half a grid interval to the *south* from $H_{j,k}$, and $U_{j,k}$ is located half a grid interval to the *east* of the $H_{j,k}$ point.

$$\begin{array}{ccccc} & & V_{j,k+1} & & V_{j+1,k+1} \\ & & \downarrow & & \\ U_{j-1,k} & \rightarrow & H_{j,k} & \leftrightarrow & U_{j,k} \leftarrow H_{j+1,k} \\ & & \uparrow & & \\ & & V_{j,k} & & V_{j+1,k} \\ & & \uparrow & & \\ U_{j-1,k-1} & & H_{j,k-1} & & U_{j,k-1} \end{array} \quad (5)$$

The grid intervals Δx and Δy are the distances between *alike* points, for instance, $U_{j,k}$ and $U_{j+1,k}$.

The numerical model we use to solve eqns (3) is designed to minimize dissipation. It incorporates a fully implicit Crank-Nicholson time step with spatial discretization of the momentum equations in the flux form, similar to Lilly's (1965) scheme for the nonlinear terms. A backward Euler time step is used for the dissipation terms.

Three features of the computational scheme are worth emphasizing:

- Following Weiyan (1992), Schär and Smith (1993) we have applied the phenomenology of the two-dimensional compressible fluids to the shallow water hydrodynamics. Both the nonlinear and the dissipation terms in the momentum equations have the form of a divergence of a *symmetric* tensor. The discrete scheme we use *retains* this property. On the *C*-grid, the diagonal elements P_{xx} and P_{yy} are defined at *H*-points, while the off-diagonal element P_{xy} is defined at vorticity points. After all of the elements of the stress tensor are computed, the second order centered finite difference approximation of the momentum equations is straightforward.

It should be mentioned that the original Lilly scheme for the nonlinear terms conserves the mean kinetic energy *exactly*. This property is based on a delicate balance of the truncation errors of the approximation of different terms and it restricts the choice of the possible discrete scheme for the nonlinear terms. In particular, in the *x*-momentum equation P_{xy} is approximated as $\bar{V}^x \bar{u}^y$, while in *y*-momentum it is represented by $\bar{U}^y \bar{v}^x$. Though both of these two expressions approximate the same term with the second order of accuracy, they are *exactly* equivalent only if the layer thickness is uniform. In this case the scheme is equivalent to the discrete Arakawa Jacobian of the third kind, which conserves the mean vorticity *exactly* (Lilly 1965). The symmetric scheme we develop here produces more accurate conservation of the potential vorticity for the case of nonuniform layer thickness, but it does not have the property of formal *exact* conservation of Kinetic energy. Consequences of this choice will be discussed later.

- As an alternative to midpoint averaging (Lilly 1965), an *asymmetric* three-point formula is used to interpolate the velocities and mass fluxes into *H* and vorticity points when computing the nonlinear terms of P_{xx} , P_{yy} and P_{xy} respectively. The additional points are always taken from the *upstream* direction, so the following expressions are used to approximate

U and V at *H* points (u and v similar):

$$\begin{aligned}\bar{U}^u &\equiv U_{j-\frac{1}{2},k} = \\ &= \begin{cases} \alpha U_{j,k} + \beta U_{j-1,k} + \gamma U_{j-2,k}, & \text{if } \bar{U}^x > 0 \\ \alpha U_{j-1,k} + \beta U_{j,k} + \gamma U_{j+1,k}, & \text{if } \bar{U}^x < 0 \end{cases} \\ \bar{V}^v &\equiv V_{j,k+\frac{1}{2}} = \\ &= \begin{cases} \alpha V_{j,k+1} + \beta V_{j,k} + \gamma V_{j,k-1}, & \text{if } \bar{V}^y > 0 \\ \alpha V_{j,k} + \beta V_{j,k+1} + \gamma V_{j,k+2}, & \text{if } \bar{V}^y < 0, \end{cases} \quad (6)\end{aligned}$$

and, at vorticity points,

$$\begin{aligned}\bar{U}^v &\equiv U_{j,k-\frac{1}{2}} = \\ &= \begin{cases} \alpha U_{j,k} + \beta U_{j,k-1} + \gamma U_{j,k-2}, & \text{if } \bar{V}^x > 0 \\ \alpha U_{j,k-1} + \beta U_{j,k} + \gamma U_{j,k+1}, & \text{if } \bar{V}^x < 0 \end{cases} \\ \bar{V}^u &\equiv V_{j+\frac{1}{2},k} = \\ &= \begin{cases} \alpha V_{j+1,k} + \beta V_{j,k} + \gamma V_{j-1,k}, & \text{if } \bar{U}^y > 0 \\ \alpha V_{j,k} + \beta V_{j+1,k} + \gamma V_{j+2,k}, & \text{if } \bar{U}^y < 0. \end{cases} \quad (7)\end{aligned}$$

To maintain second order of accuracy, coefficients α , β , γ in (6) and (7) must satisfy

$$\alpha + \beta + \gamma = 1, \quad \alpha - \beta = 3\gamma,$$

and, therefore, there is only one free parameter among α , β , γ . Let

$$\alpha = \frac{1}{2} + \gamma, \quad \beta = \frac{1}{2} - 2\gamma,$$

and γ is the adjustable parameter.

Analysis of the truncation error shows that, for example,

$$\begin{aligned}\delta(P_{xx}) &= \frac{\partial P_{xx}}{\partial x} + \text{sign}(U)(\Delta x)^2 \times \\ &\times \left\{ \left(\frac{1}{6} + \gamma \right) \left[u \frac{\partial^3 U}{\partial x^3} + U \frac{\partial^3 u}{\partial x^3} \right] + \right. \\ &\quad \left. + \left(\frac{1}{4} + \gamma \right) \left[\frac{\partial u}{\partial x} \frac{\partial^2 U}{\partial x^2} + \frac{\partial U}{\partial x} \frac{\partial^2 u}{\partial x^2} \right] \right\} + \\ &\quad + \mathcal{O}((\Delta x)^3) \quad (8)\end{aligned}$$

where $\delta(\dots)$ is the usual centered difference operator. The first term in curly brackets may be interpreted as numerical dispersion in the nonlinear terms, while the second term corresponds to the numerical dissipation in the nonlinear terms. No choice of the upstream parameter γ can eliminate both terms in curly brackets; however, we see that introduction of the upstream scheme may drastically reduce the truncation error in comparison with the original Lilly scheme with $\gamma = 0$. In the present study we set $\gamma = -1/8$, which corresponds to the third order of accuracy approximation

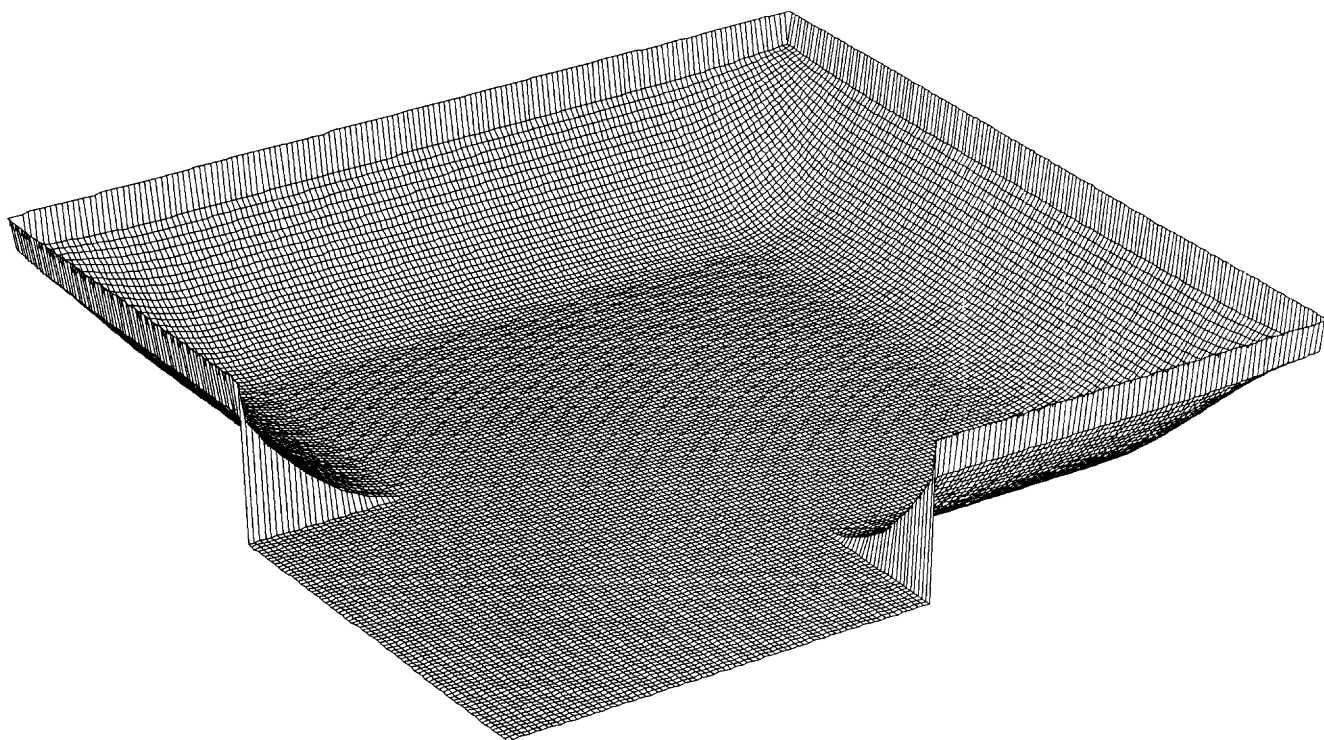


Figure 1. Perspective view of the bottom topography for all four cases. The quarter of the domain closest to the viewer has been lowered down to the deepest value for illustrative purpose. The actual topography is symmetric and has continental slopes along all four sides. The shape of the slope can be easily seen on the cross sections. The minimum depth near the sides is 20% of the deepest value in the middle.

for the nonlinear part of the stress tensor. Though not the best from the point of view of (8), this choice virtually eliminates aliasing errors caused by the subsequent use of spatial averaging and finite differencing of the averaged values. Consequently, the asymmetric scheme does not generate spurious enstrophy cascades to small scales and, therefore, requires a relatively small explicit dissipation to keep the numerical stability.

- The *method of artificial compressibility* is employed to implement the fully implicit time step (Tukel 1987, Gresho and Sani 1987, Soh and Goodrich 1988, Weiyan 1992, Alcubierre and Schutz 1994, Marx 1994). This approach is based on introducing an internal *pseudo-time* and special relaxation procedure between *physical* time steps to obtain the solution. The iterative procedure starts from a second order explicit predictor in *physical* time to obtain the initial approximation for the new time step fields. After that several *ADI*-type split-implicit substeps in *pseudo-time* are applied to obtain the pressure field at the new time step and correct the solution. The time step is unconditionally stable with respect to

fast surface gravity waves, can formally be applied to the incompressible limit $g = \infty$, and allows an implicit representation of the nonlinear and dissipation terms. In comparison with the more common three time level semi-implicit version of Kwizak and Robert (1971), the new approach leads to four times smaller truncation errors in the time differencing of both nonlinear and pressure terms. The computations presented here are performed on a 301×301 grid. The nonlinear terms are recomputed 3 times per every *physical*-time step, and $8 \approx \log_2 300$ *ADI* iterations are required to correct the pressure field every time after the nonlinear part is recomputed.

The Topographic Engine Experiment

Because our purpose is to investigate the possibility of conversion of energy from random flow into large scale *rectified* motion, i.e., in thermodynamical terms, from *heat* into *mechanical* energy, we refer to this part of the study as the *topographic engine* experiment. In the present section we discuss several experiments with free decaying shallow-water turbu-

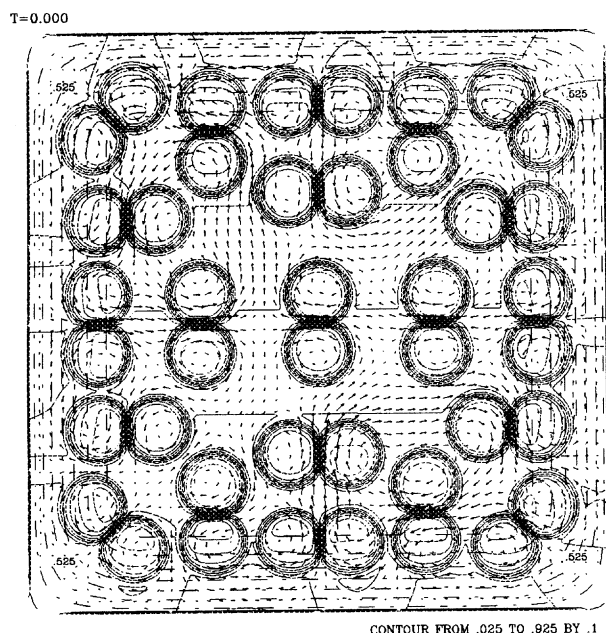


Figure 2. The initial state. The potential vorticity field is shown in contours, while arrows represent velocities. Only every sixth vector is plotted. Note that the initial flow is composed of dipoles and has no specific symmetry. Also, there is no net circulation around the box.

lence in the presence of bottom topography. All of the cases presented here have the same domain geometry and bottom topography shown in Figure 1. The bottom is flat in the middle of the basin and rises near the sides, which simulate the continental slopes. No-slip boundary conditions are imposed on the sides of the rectangular domain.

To specify the initial state, we prescribe the potential vorticity field (f -plane case, see below) or relative vorticity field (β -plane cases), solve the elliptic problem to obtain the streamfunction, and, finally, the mass fluxes of the initial state, which is always assumed to be nondivergent. The (potential) vorticity field of the initial state is always composed of randomly oriented dipoles, so that there is no net circulation around the box (Fig. 2). There is no forcing in any of our experiments.

All computations are performed for nondimensional variables where we set different values of the nondimensional Coriolis parameters and keep all other nondimensional parameters unchanged. To get some impression about the correspondence of our experiments to the dimensional world, the four experimental setups may be identified as follows:

- The first case, hereafter referred as the f -plane case, corresponds to a domain of 500×500 km at 45°N . The Coriolis parameter $f = 10^{-4}\text{sec}^{-1}$ is assumed to be uniform. With velocity scale $V = 1$ m/sec and the advection time scale $T = L/V = 5 \times 10^5 \text{ sec} \approx 6$ days, the non-dimensional Coriolis frequency is

$$\mathcal{F} = \frac{fL}{V} = 50$$

Grid resolution is 301×301 for the all cases presented here.

- **Weak β -case**

$$\mathcal{F}(y) = \mathcal{F}_0 + \beta \frac{y}{L} = 50 + 50 \left(\frac{y}{L} - \frac{1}{2} \right)$$

- **Moderate β -case**

$$\mathcal{F}(y) = \mathcal{F}_0 + \beta \frac{y}{L} = 150 + 150 \left(\frac{y}{L} - \frac{1}{2} \right)$$

- **Strong β -case** The domain size is 3000×3000 km (from 20°N to 50°N). A velocity scale of $V = 0.5$ m/sec gives

$$\mathcal{F}(y) = 400 + 400 \left(\frac{y}{L} - \frac{1}{2} \right)$$

The advection time scale $6 \times 10^6 \text{ sec} = 70$ days

The results of the computations are presented in Fig. 3 – Fig. 6. (See also captions for additional discussion.)

The f -plane experiment: To compare the upstream scheme with the original centered difference Lilly scheme, we run the f -plane case twice, using both schemes. All of the conditions are the same, except for the viscous coefficient A . The Reynolds number (based on the domain size) is 10^{+4} for the centered difference case, which is nearly on the edge of the numerical stability for this numerical scheme. Note that the Reynolds number is $3 \times 10^{+5}$ (which is 30 times larger) for all other experiments, when the upstream scheme is used to discretize the nonlinear part of the momentum flux tensor. We did not find any tendency to produce grid size scale oscillations when the upstream version is used. Despite the larger dissipation, the centered difference solution (not shown here) is much noisier, dissipates kinetic energy faster and does not result in a monotonic decay of potential enstrophy. However, the physical behaviour of the flow is similar for both cases. The experiments show that the turbulent flow tends to organize itself

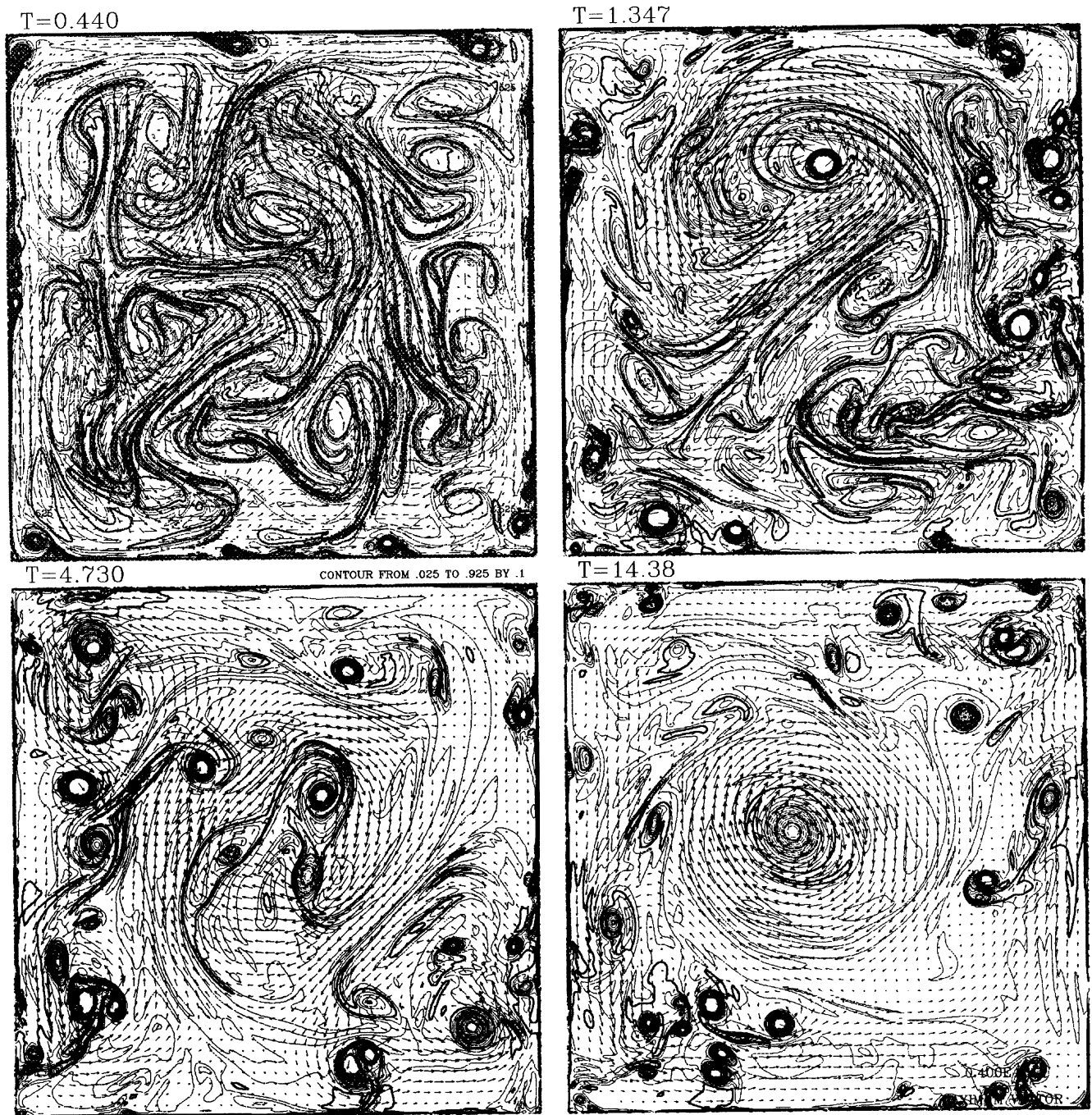


Figure 3. Temporal evolution of the potential vorticity field from the initial state shown on Fig. 2 for the case of an f -plane. Time is scaled by the advection time scale. The upper left panel shows the potential vorticity and velocity field shortly after the beginning. All the original dipolar structures are rapidly destroyed. At the same time, there is formation of new compact eddies near the walls. These eddies may have amplitudes of relative vorticity anomaly larger than the original field. The anticyclonic vorticity tends to concentrate in the middle of the basin, while cyclones are more likely to stay in the shallower regions near the sides. Note the formation of the cyclonic circulation around the box near the boundaries (lower right panel).

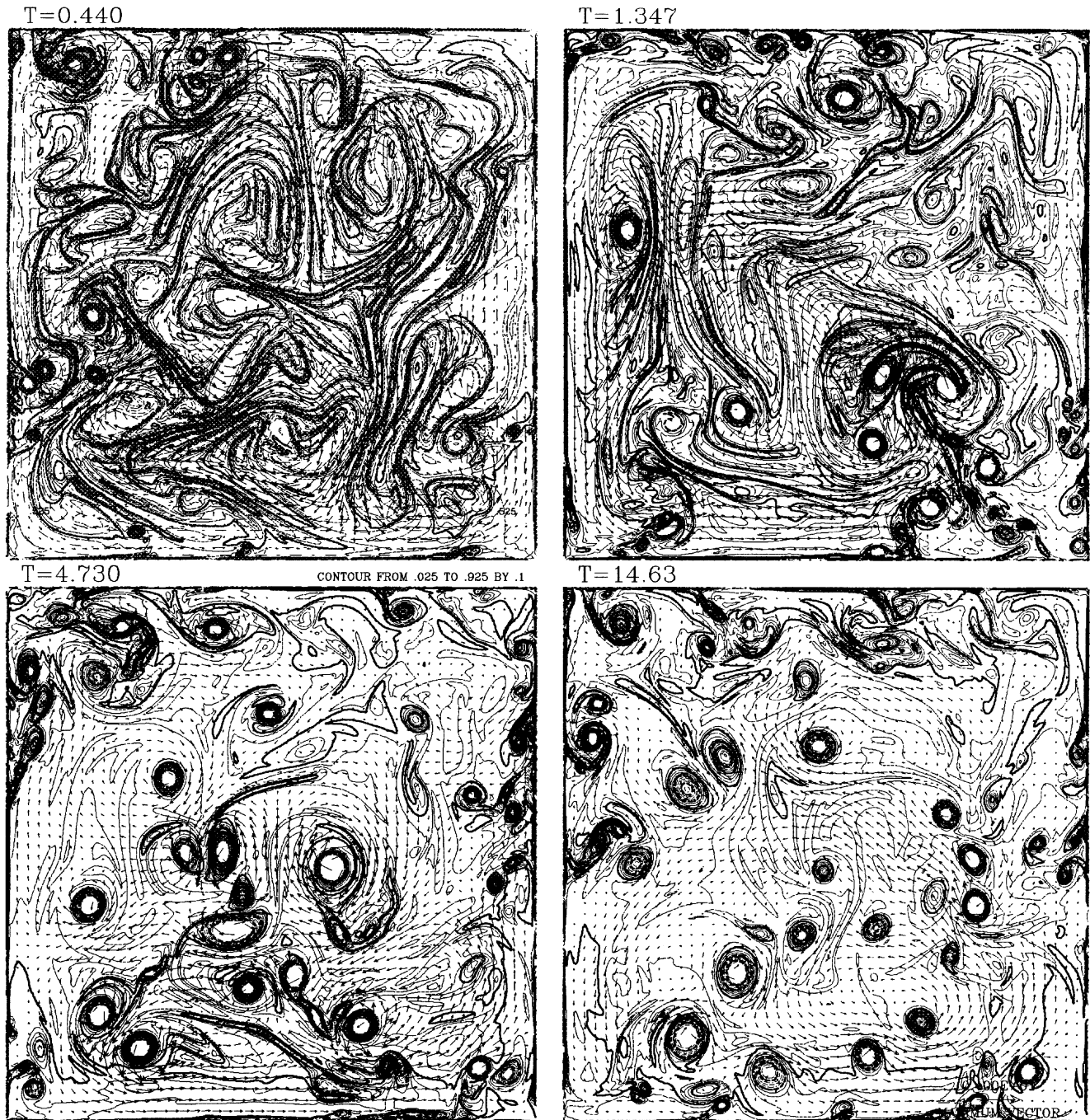


Figure 4. Case of weak planetary β -effect. In this regime the β -effect is not strong enough to either restrict fluid motion in the meridional direction, or to cause decay of mesoscale eddies via radiation of Rossby waves. However, it restricts the size to which the coherent structures may grow. Notice the presence of many small intense eddies in the middle of the domain instead of a large scale merged core, as seen in Fig. 3. There is also evidence of the development of a rectified cyclonic circulation around the domain (bottom right panel).

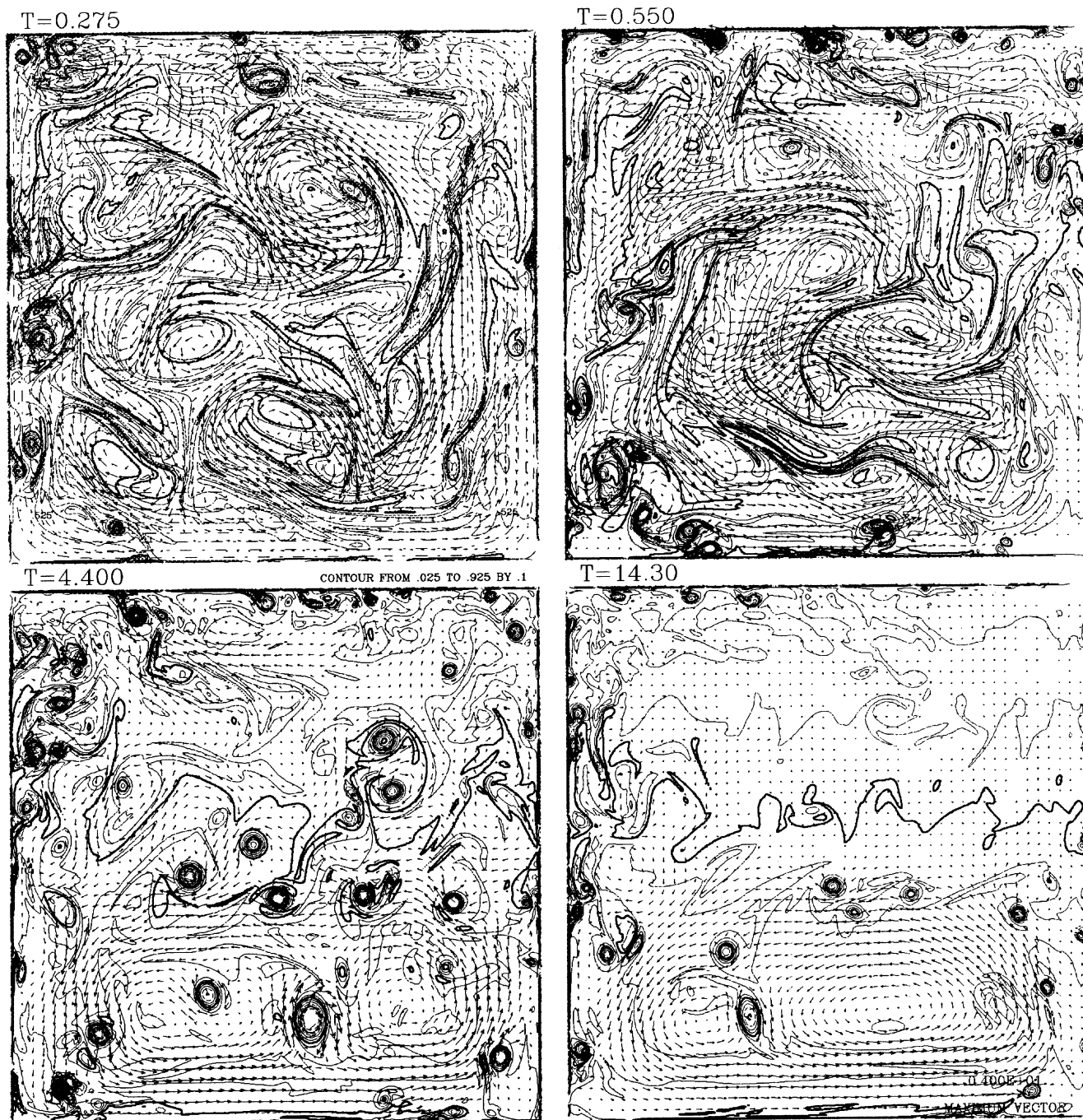


Figure 5. Case of intermediate planetary β -effect. The β -effect is now stronger and decay of mesoscale features due to radiation of Rossby waves becomes more evident. Time is scaled by the advection time scale. Note that these four snapshots are taken at times different from those of the two previous cases. This flow has north-south as well as east-west asymmetry, which were practically absent in the previous two experiments. Rectified circulation intensifies near the southern part of the domain and it detaches from the eastern coast. The separation point becomes also the place where anticyclonic eddies leave the coast and are advected into the interior of the basin, where they eventually will be destroyed by the β -effect. The cyclonic eddies remain topographically arrested and tend to propagate along the eastern coast to the north. Note the appearance of an east-west alignment of eddies as well as a restriction of the fluid motion in the meridional direction.

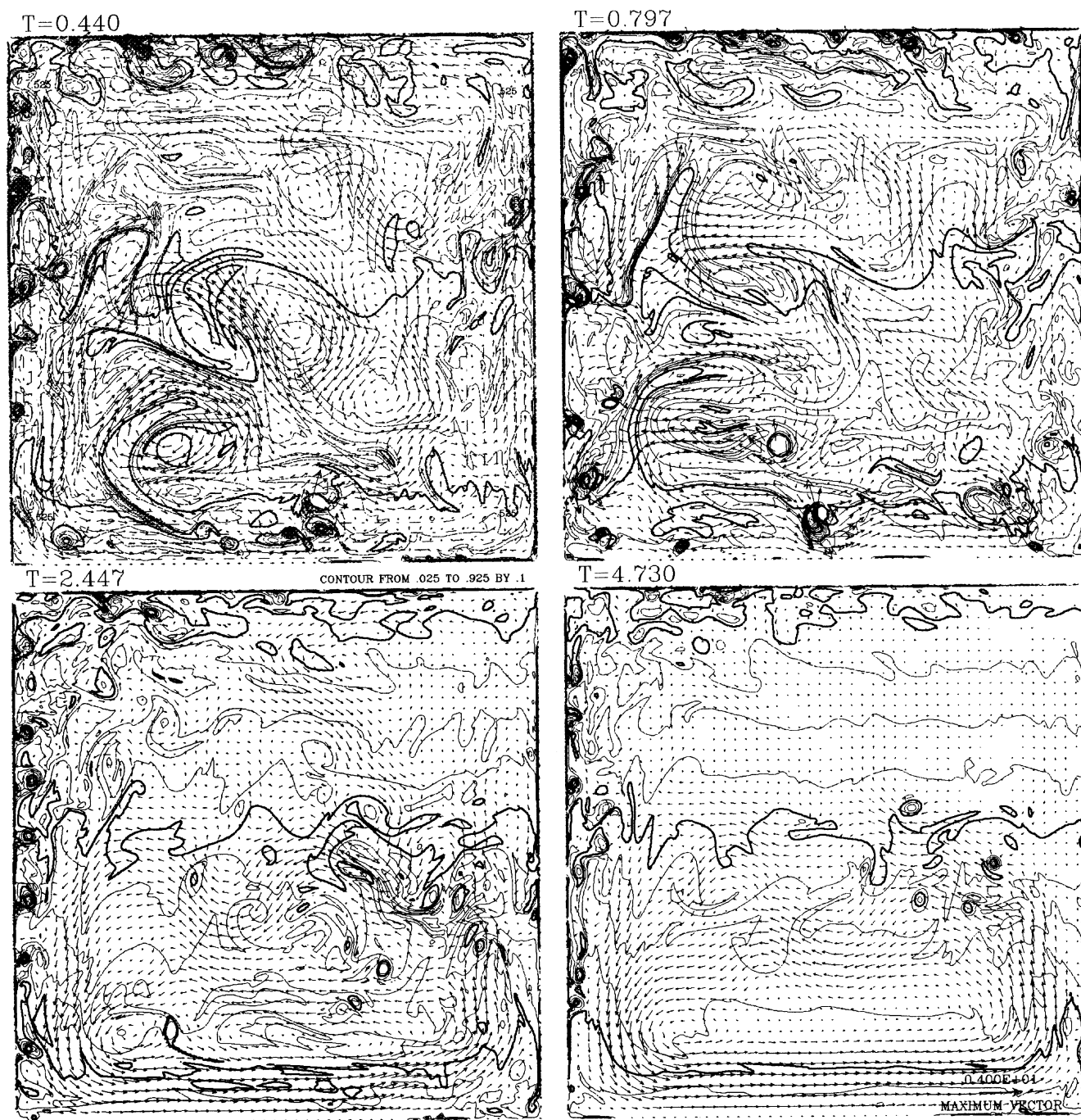


Figure 6. Case of strong planetary β -effect. In this case the meridional change of the Coriolis parameter dominates the relative vorticity anomalies associated with the initial random eddy field. Consequently, the original structures were immediately destroyed. Both the east-west and the north-south asymmetries are more pronounced than in the previous case. There is formation of both cyclonic and anticyclonic eddies near the western coast, but both the planetary β -effect and bottom topography prevent them from being injected into the interior of the basin. Note formation of the intense jet along the southern boundary and recirculation gyre. As in the previous case, we see injection of small scale eddies at the flow separation point on the eastern coast.

into a current along the perimeter of the basin in the counter-clockwise direction, while the negative vorticity tends to concentrate in the middle of the domain (Fig. 3). In classical numerical simulations of free-decaying two-dimensional turbulence there is no process opposite to the vortex merger and, therefore, no small scale structures can be created from large scale structures. In our case, in contrast, there is generation of small scale structures on the no-slip boundaries. Injection of fresh, intense and compact new eddies into the interior of the domain enhances mixing of the low-vorticity anomalies of old vortices. Consequently we observe a relatively uniform potential vorticity background field with several small scale intense coherent structures embedded in it. In this situation, regardless of the details of the initial state, the spatial spectrum of the turbulent flow rapidly reaches some equilibrium state, which persist during a relatively long period of time (bottom left panel of Fig. 3).

Due to the presence of continental slopes and Coriolis effect, the anti-cyclonic eddies are more likely to be driven into the interior of the domain, while anti-cyclones tend to stay near the walls. This can be explained by potential vorticity conservation and the energetics of the flow: moving a cyclonic vortex core from a shallow to a deep region causes its spin up:

$$PV = \frac{f + \omega}{H} = \text{const}, \quad f > 0, \quad \omega > 0$$

$$\left. \begin{array}{l} f \rightarrow \text{conserved} \\ H \rightarrow \text{increases} \end{array} \right\} \Rightarrow \omega \rightarrow \text{increases}$$

The kinetic energy associated with an eddy is

$$KE \sim Vol \cdot \omega^2 r^2 \sim Vol^2 \frac{\omega^2}{H} \sim \omega \cdot \frac{\omega}{H},$$

where $Vol \sim r^2 H$ is the characteristic volume of the vortex core, while r is its radius. Obviously Vol is conserved and both ω and the ratio ω/H increase due to the conservation of potential vorticity. Consequently, the kinetic energy has to increase when a cyclonic core is driven from the shallow to deeper regions. Thus, an external flow *must* produce some work on order to move the core.

Similar considerations may be made for the anti-cyclonic vortices, where ω and f are of different signs. It turns out that there is no energetic barrier for the anti-cyclones to leave the coast. For example, zero potential vorticity eddies, $\omega = -f$, are not sensitive to the vortex stretching at all, while they may even

release some amount of kinetic energy when H is increasing. On the other hand, assuming some dissipation in the system, one can see that the process of redistribution of the vorticity field becomes *irreversible* in the sense that once an anti-cyclonic eddy leaves the coastal region, it cannot come it back, unless it is pushed by the background flow.

Weak β -effect case. The most noticeable difference from the previous case is the behavior of the turbulent flow in the interior. To some extent, the β -effect inhibits the merging process inside the domain and restricts the size to which the eddies can grow (Rhines rule). There is no evident decay of single eddies due to radiation of Rossby waves. There is some evidence of the meridional restriction of the motion and east-west as well as north south asymmetry of the flow.

Intermediate β -effect case. The differences from the previous case are these: there is evident decay of eddies due to radiation of Rossby waves. The motion tends to be meridionally restricted. The organized flow around the box is intensified in the southern part of the basin, while the northern part exhibits predominantly wave type motion rather than turbulent eddy flow.

Strong planetary β -effect. Rapid decay of initial eddies is due to radiation of Rossby waves. There is an evident formation of the organized flow with the strong jet along the southern boundary.

For the all four cases the decay of the mean kinetic energy is shown in Figure 7, while Figure 8 shows time evolution of the mean potential enstrophy. The kinetic energy is normalized by its initial value, so all curves on Figure 7 start from $KE = 1$ and monotonously decay. The lowest curve corresponds to the dissipative centered difference scheme. It is presented here only to demonstrate difference between the two numerical schemes. For physical considerations it should be ignored. From the other four curves one can conclude that presence of β -effect generally enhances dissipation. This result may require additional investigations, because for the case of unbounded freely decaying geostrophic turbulence (doubly periodic domain) there is an opposite tendency: radiation of Rossby waves in a periodic domain does not dissipate energy, while the eddy mixing process (which causes eddy merging and filamentation – the main dissipative mechanism) tends to be suppressed (Rhines and Young 1982b). The difference may be explained by the presence of no-slip boundaries.

Before interpreting Figure 8, it should be explained

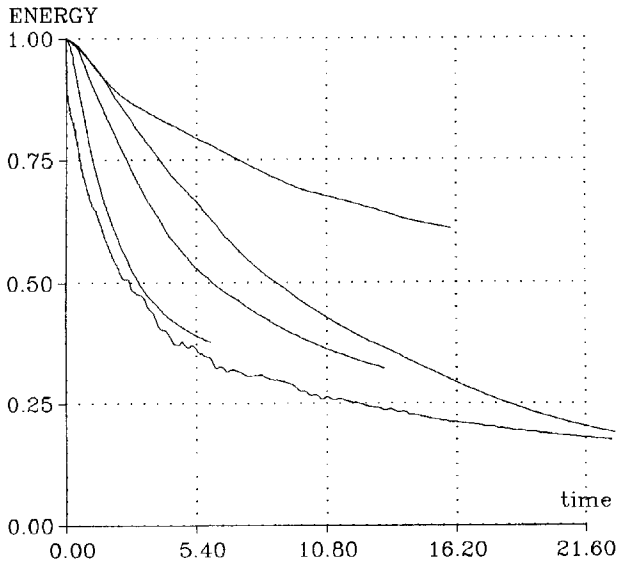


Figure 7. Time decay of the kinetic energy (KE) integral for all four different experiments. The KE is normalized by its initial value. The five curves, starting from the highest, correspond to the f -plane upstream case (terminates at $t = 16.20$); weak planetary β -effect case (goes beyond $t = 21.60$); intermediate β (terminates at $t = 13.5$); strong β (terminates at $t = 5.8$); f -plane case when centered scheme was used (goes beyond $t = 21.60$).

that the mean enstrophy is defined as

$$\langle q \rangle = \left\langle H \cdot \frac{1}{2} P V^2 \right\rangle = \left\langle \frac{(f + \omega)^2}{2H} \right\rangle, \quad (9)$$

where $\langle \dots \rangle$ denotes the integration over the domain. For a given initial state we may define the initial value of the potential enstrophy $q_0 = q(t = 0)$, and the mean potential enstrophy of the rest state

$$q_{\text{rest}} = \left\langle \frac{f^2}{2H_{\text{rest}}} \right\rangle. \quad (10)$$

Figure 8 shows the function

$$q^* = \frac{q(t) - q_{\text{rest}}}{q_0 - q_{\text{rest}}}. \quad (11)$$

Obviously, this function is the normalized mean potential enstrophy. In the case of a closed system, when no potential enstrophy can be generated on the boundary or brought in through the boundary, this quantity must be conserved if there is no internal dissipation. It monotonously decays from 1 to 0 if dissipation is present.

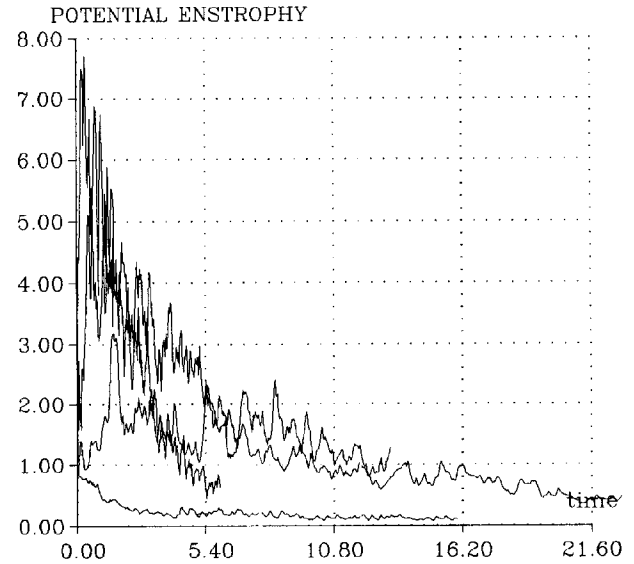


Figure 8. Potential enstrophy integral as the function of time for all four cases. The four curves (f -plane centered difference case is not shown) may be identified by the length of the curve, similar to the previous figure.

In the case when vorticity (and, consequently, enstrophy) may be created on the boundary, the behaviour of this integral is not so evident. It is interesting to note that in the f -plane case it decays practically monotonously. All β -plane cases may be characterized by an initial burst and a subsequent decay. We suggest that the initial state is very far from the dynamical equilibrium in the β -plane cases, so, shortly after the beginning, the flow tends to readjust itself to bring all fluid parcels to their equilibrium latitudes. This process takes place mostly in the interior of the domain and causes generation of strong shear near the boundaries, which results in the generation of small scale turbulence, which becomes the major contribution to the enstrophy integral. After this readjustment enstrophy decays.

Final Remarks

For the conclusion, we summarize several observations:

- Due to the presence of the no-slip boundaries there is generation of the small scale features which oppose the merging of sign-like eddies in the interior of the basin.
- In the presence of topography on an f -plane, the turbulent flow tends to organize a rim current around the domain and concentrate negative vorticity in the

middle.

- Coupling of bottom topography and Coriolis effect causes *cyclone-anticyclone asymmetry*, even in the case when the Rossby number is small.

- Migration of the eddies along the wall can be explained by *image effect*, topographic β -effect, planetary β -effect and interaction with the viscous boundary layer. Anti-cyclonic eddies are more likely to be ejected into the interior of the domain, while cyclones tend to be coastally trapped. This effect can be explained in terms of conservation of the potential vorticity and energetic consideration.

- A weak planetary β -effect partially inhibits the merger process inside the domain. Rhines (1975) rule may also be applied to the case of ageostrophic dynamics.

- In the presence of topography, both weak and strong planetary β -effects make the anti-cyclonic eddies more likely to separate from the coast than in the case of an f -plane.

- The planetary β -effect causes asymmetry of the rectified flow with intensification of southern boundary currents, which results in configuration of the flow similar to Fofonoff's southern mode inertial boundary current.

- There is an east-west asymmetry in the boundary current behavior (Figs. 5 – 6).

- There is a topographic instability of northward flowing eastern boundary current and cyclone-anticyclone separation near the eastern coast.

From these numerical experiments we see that the *rectification* process is associated with several physical phenomena, such as vortex stretching and turbulent mixing, which are affected by the topography itself as well as by planetary vorticity gradients and lateral friction, which also allows generation of vorticity on the boundaries. This study shows that, in principle, ocean models are capable to simulate this behavior directly, however, at a high computational cost. Parametrization of this effect is desirable, but not obvious. In particular, this effect has *nonlinear* and *nonlocal* nature, so that the statistical equilibrium velocity at some particular point depends on the *global* field, rather than on the local bottom slope and Coriolis parameter. One can expect this keeping in mind the inherent elliptic properties of the barotropic flows. Parametrizations based on variational principles seem to be more attractive.

One should recall that in numerical simulation of the geophysical flows there is a tendency to gener-

ate finer and finer scales when the grid size and the lateral viscous coefficient decrease, rather than going to a computational regime when the fields become smooth on the grid scale. This classical mathematical convergence is practically never achieved. This motivates the design of numerical schemes which produce well behaved solutions in all scales up to the grid size. In many cases, special properties, such as non-generation of spurious cascades of enstrophy in small scales as well as properties of monotonicity (i.e. non-generation of spurious minima and maxima), may be more valuable than the formal order of the mathematical convergence. Because there are many desirable properties and no one computational design can reproduce all of them, a compromise should be made. The scheme used in the present study is an example of such a compromise: despite the formal loss of the conservation of kinetic energy in the nonlinear terms, the better cascade properties allow the use of a smaller explicit dissipation. As a result, the model has better *overall* energy conservation than the model which uses the centered scheme.

Acknowledgments. COAPS receives its base support from the Secretary of NAVY Research Grant N00014-85-J-1240 from the Office of Naval Research. This research was also supported by the Advanced Research Projects Agency (ARPA) grant SC25046. Special thanks to Prof. J. J. O'Brien for his support and advise. The author is grateful to Dr. Wesley Jones, Dr. Detlev Müller, Dr. Steven Meyers, Dr. George Sutyrin and Dr. Eduard Zuur for the numerous discussions at several stages of this work. Computations were performed on Florida State University CRAY Y-MP. Special appreciation to Nancy Kellett for her support and patience.

References

- Alcubierre, M. and B. F. Schutz, 1994, Time-Symmetric ADI and Causal Reconnection: Stable Numerical Techniques for Hyperbolic Systems on Moving Grids, *J. Comput. Phys.*, **112**, 44-77.
- Alvarez, A., J. Tintore, G. Holloway, M. Eby and J. M. Beckers, 1994, Effect of topographic stress on the circulation in the western Mediterranean, *J. Geophys. Res.*, **99**, 16053-16064.
- Carnevale, G. F. and J. S. Frederiksen, 1986, Nonlinear stability and statistical mechanics of flow over topography, *J. Fluid Mech.*, **175**, 157-181.

- Cummins, P. and G. Holloway, 1994, A note on eddy-topographic stress representation, *J. Phys. Ocean.*, **24**, 700-706.
- Eby, M. and G. Holloway, 1994, Sensitivity of a large scale ocean model to a parameterization of topographic stress, *J. Phys. Ocean.*, **24**, 2577-2588.
- Gresno, P. M. and R. L. Sani, 1987, On the pressure boundary conditions for the incompressible Navier-Stokes equations, *Int. J. of Num. Meth. in Fluids*, **7**, 1111-1145.
- Holloway, G., 1986, Eddies, waves, circulation and mixing: statistical geofluid mechanics, *Ann. Rev. Fluid Mech.*, **18**, 91-147.
- Holloway, G., 1992, Representing topographic stress for large scale ocean models, *J. Phys. Ocean.*, **22**, 1033-1046.
- Holloway, G. and M. Eby, 1994, Exercising a Hybrid Statistical Mechanics - Ocean circulation model, research activities in atmospheric and oceanic modelling, 19, G. J. Boer, ed., WMO, Geneva
- Kwizak, M., A. J. Robert, 1971, A semi-implicit scheme for grid point atmospheric models of the primitive equations, *Mon. Weather Rev.*, **99**, 32-36.
- Lilly, D. K., 1965, On the computational stability of the time-dependent non-linear geophysical fluid dynamics problem, *Mon. Weather Rev.*, **93**, 11-26.
- Marx, Y.P., 1994, Time integration schemes for the unsteady incompressible navier-stokes equations, *J. Comput. Phys.*, **112**, No 1.
- Rhines, P. B. 1975, Waves and turbulence on a beta-plane, *J. Fluid Mech.*, **69**, 417-443
- Rhines, P. B. and W. R. Young, 1982a, A theory of the wind-driven circulation. I: Midocean gyres, *J. Marine Res.*, **10(3)**, 559-596.
- Rhines, P. B. and W. R. Young, 1982b, Homogenization of potential vorticity homogenization planetary gyres, *J. Fluid Mech.*, **122**, 347-368
- Salmon, R., G. Holloway and M. C. Hendershott, 1976, The equilibrium statistical mechanics of simple quasigeostrophic models, *J. Fluid Mech.*, **75**, 691-703.
- Soh, W. Y. and J. W. Goodrich, 1988, Unsteady solutions of incompressible Navier-Stokes equations, *J. Comput. Phys.*, **79**, 113-134.
- Schär, C. and R. Smith, 1993, Shallow water flow past isolated topography. Part I: Vortex production and wake, *J. Atmosph. Sci.*, **50**, 1373-1401.
- Thompson, L-A, 1993, The effect of continental rises on the wind-driven ocean in an eddy resolving model, *Proceedings of XIXth Conference on Atmospheric and Oceanic Waves and Stability*, San-Antonio, Texas, 1992.
- Turkel, Eli, 1987, Preconditioned methods for solving the incompressible and low speed compressible equations, *J. Comput. Phys.*, **72**, 277-298.
- Weiyen, T., *Shallow Water Hydrodynamics*, Elsevier Science Publishers, Hong Kong, 1992